ORIGINAL ARTICLE

Study of 40Cr surface modification grinding force and temperature based on microstructure evolution mechanism

Yunlong Yao[1] · Cong Sun[1] · Shichao Xiu[1] · Yuan Hong[1] · Zhuangzhuang Hou[1] · Xiannan Zou[1]

Abstract

Aiming to improve the dynamic and static contact performance of 40Cr alloy parts, a grind-strengthening (GS) compound process is applied to the finish machining and surface quenching heat treatment of 40Cr alloy steel, which makes the material undergo a modification behavior of dynamic phase transformation introduced by high grinding heat and severe plastic deformation (SPD). The microstructure evolutions of material during the GS process comprise dynamic recrystallization (DRX) and phase transformation. The flow property of material can be critically affected by microstructure transformations during the GS process, which has a significant impact on the grinding force and temperature. A modified Johnson–Cook (J-C) constitutive equation considering grain size was established in this study. The flow stress can be calculated by the model during machining and the grinding force can be predicted. Moreover, the grinding temperature can be calculated by an analytical model according to the predicted grinding force. In addition, the grind-strengthening experiment was conducted. The applicability of the modified J–C model can be verified. The results show that the grinding forces obtained by the modified J–C model are more accurate. Furthermore, by comparing the prediction of temperature field distribution and the gradient microstructure introduced by dynamic phase transformation of the ground strengthening layer, the prediction of grinding temperature based on the analytical method is consistent with the experiment results. And the creation mechanism of grind-strengthening layer can be revealed profoundly.

1 Introduction

A principal objective of grind strengthening is the creation of a strengthened surface after removing materials with specific attributes that enable the functional machining of products. Grind-strengthening technology can be used to obtain a modified superficial layer with high microhardness and high strength caused by phase transformation and dynamic recrystallization under high grinding temperature, high strain, and strain rate conditions [1–3]. From the surface integrity perspective, the microstructure evolution of ground surface and subsurface is perhaps the most critical since it determines mechanical and physical properties [4, 5].

40Cr, a typical low-alloy structural steel, composed of pearlite and ferrite is commonly used as the essential parts including gears, shafts, sleeves, and connecting rods as examples. The service performances of the components are extremely dependent on the finish machining method, and grinding is a frequently applied process solution. Moreover, grind-strengthening technology, as a green and efficient finish machining method, utilizes the high heat and SPD to result in austenite transformation of material, and air cooling is applied for the heat treatment of quenching [6]. In comparison, traditional grinding is difficult to achieve this composite strengthening function. Zarudi and Zhang [7] further studied the microstructure transformation mechanism of hardened steel during the grinding process. It can be stated that the changes in temperature, stress, crystallographic structure, and dislocations have a critical impact on the transformation of the material microstructure. And the higher cooling rate and SPD can inhibit the appearance of ferrite and bainite, which also can refine austenite

✉ Shichao Xiu
  shchxiu@mail.neu.edu.cn

[1] School of Mechanical Engineering and Automation, Northeastern University, Shenyang 110819, China

grains and ultimately precipitate the formation of fine martensite [8]. In the past several years, in addition to the phase transformation, many researchers have developed a strong passion for the investigations of dynamic recrystallization behavior during the hot processing of steel. The DRX model was established based on the hot compression tests of 40Cr [9]. It provided a strong foundation for studying the DRX behavior during thermal deformation of 40Cr steel. Duan et al. [10] investigated the microstructure evolution mechanism of AISI1045 and AISI52100 during the hard cutting process. It pointed out that the grain refinement is caused by phase transformation and dynamic recrystallization behavior due to high cutting heat and SPD. The finite element analysis was applied to predict the cutting force and temperature with the comprehensive consideration of coupling effect of thermal–mechanical and phase transformation metallurgy. And the established model was validated by cutting experiments. In addition, concerning the fully hardened steel material under drilling conditions, it was noted that the white layer of the drilling surface was a combination of the phase transformation and the grain refinement caused by the drilling heat and severe plastic deformation [11, 12]. Hence, there is another important style for the modification of the machined surface, which is the grain refinement mechanism in addition to the phase change mechanism.

In recent years, the investigations of grain refinement surfaces created by the machining process have aroused widespread interest and attention. Grain refinement is known as an excellent strengthening method to enhance comprehensive mechanical properties [13, 14]. During the supercritical carbon dioxide (scCO2)-assisted grinding process of ultrahigh strength 300 M steel [15], dry and cryogenic cutting of AISI4340 steel [16], the laser shock peening process [17], dry and minimum quantity lubrication grinding of single-crystal nickel-based superalloys [18], there was obvious grain refinement behavior in the machined superficial layer. The research results indicated that grain refinement can not only make an outstanding contribution to the microhardness but also can form residual compressive stress on the machined surface and improve the wear resistance of the part surface. Tsuji and Maki [19] discussed three-grain refinement mechanisms incorporating phase transformation and SPD for steel: (a) phase transformation after SPD, (b) phase transformation prior to SPD, and (c) reduplicate SPD and phase transformation. These three mechanisms of grain refinement have the potential to create new nanostructured materials and discover new metallurgical phenomena.

The microstructure evolutions including dynamic recrystallization and phase transformation have a crucial influence on the mechanical force and the surface residual stress during the machining process [20]. Pan et al. [21, 22] proposed a cutting force prediction model considering the effects of DRX. The prediction accuracy had been improved. Zhang

et al. [23] believed that material separation is primarily caused by the comprehensive impact of mechanical shear and thermally driven microstructure transformation during the cutting of titanium alloys. Because the flow stress is greatly affected by the phase component. Therefore, a constitutive model considering phase transformation was established, which can effectively predict chip separation and microstructure distribution. Ding et al. [24] studied the mechanism of microstructure transformation impact on the micro-grinding force during machining maraging steel. A hybrid iterative model coupling phase transformation kinetics and grinding mechanics was developed. The results showed that the established model had high applicability. The influence of microstructural transformations on grinding process was better understood. Therefore, the plastic flow deformation and removal of heterogeneous materials during the machining process are closely related to the microstructure. In this study, 40Cr alloy steel was machined by strong grinding parameters to achieve ground superficial layer modification. As a result, the grind-strengthening process integrates almost simultaneously phase transformation and dynamic recrystallization to obtain ultra-fine grained and high strength-toughness creation surfaces [25]. Hence, it is necessary to study the impact of microstructure evolution on grind strengthening. These previous studies have indeed done more in-depth and basic research on the microstructure evolution mechanism of steel during thermal deformation processes such as phase transformation, DRX, and SPD during the cutting, drilling, and milling process. However, there are few reports on the feedback influences of theoretical models of material microstructure evolution on deformation resistance and heat generation during the grinding process. Hence, the grain refinement behavior during the grind-strengthening process leading to the variety of the yield strength of the material and affecting the changes of force and heat can be researched in this study for revealing the influence of microstructure on the grinding process.

In the compound process of grind strengthening, the microstructure modifications resulting from the grinding heat and SPD occur in the material deformation zone. The modification of materials could significantly influence the flow stress and macro-grinding force in the process of grind strengthening. Firstly, due to the material being removed by the abrasive particles with a negative rake angle geometry, the strain and strain rate can be calculated by the slip line analysis model [26]. Then, considering the grain refinement phenomenon in the material thermal deformation processing, the material grain size can be predicted by Johnson-Mehl- Avrami-Kolmogorov model through strain, strain rate, grinding temperature, and flow stress. A modified J–C model based on dynamic recrystallization grain refinement was established. The material flow stress and grinding force are calculated based on the variations in grain size. Finally,

the grinding temperature can be solved according to the analytical model with the triangular moving heat source based on the microstructure evolution. The predicted grinding force and temperature are verified by grind-strengthening experiments. In comparison to the traditional J–C model, the effectiveness of considering grain size influence on the improvement of existing model is verified.

2 Constitutive model of material based on grain size

Grind-strengthening technology, a green and efficient dry grinding method, integrates the finish machining and surface hardening heat treatment. The material undergoes austenitization and dynamic recrystallization transformation caused by elevated grinding heat and SPD during grinding. Therefore, the ground surface of grain refinement martensite can be formed by dynamic recrystallization transformation and air cooling during the grind-strengthening process. It can be used to obtain an excellent machined surface. The schematic diagram of microstructure evolution and grain refinement mechanism of the grind-strengthening layer is explained in Fig. 1. The reduction of prior austenite grains can lead to the increase of transformation driving force, the density of high-angle grain boundary, and martensite content. Thus, the comprehensive mechanical properties of the material are improved. The strengthening mechanism of the prior austenite grain refinement can be analyzed according to the classic Hall–Petch relation [27]:

$$\begin{aligned} \sigma_y &= \sigma_0 + K_y d^{-1/2} \\ \sigma_c &= \sigma_{c0} + K_c d^{-1/2} \\ T_B &= T_{B0} - K_B d^{-1/2} \end{aligned} \tag{1}$$

where σ_y, σ_c, and T_B are the yield strength, crack growth resistance, and ductile–brittle transition temperature, respectively. σ_0, σ_{c0}, and T_{B0} are material constant. K_y, K_c, and K_B are the Hall–Petch coefficients, and d is the grain size of prior austenite. It can be seen from Eq. (1) that the refinement of the prior austenite grains has a positive effect on the strength and toughness of the material, and it also reduces the ductile–brittle transition temperature. A decrease in the size of martensite and an increase in the dislocation density within the martensite can be caused by the refinement of the prior austenite grains [28]. The enhancive dislocation density is the essential reason for the strengthening of austenite refinement. Therefore, the grain refinement mechanism can not only improve the strength but also improve the plasticity and toughness of the material, which is of great application value to the balance of strength and toughness of steel.

The microstructural modification and grain refinement on the material plastic deformation zones are produced by thermal–mechanical phase transformations and DRX behavior. The flow characteristic of material can be changed. The DRX grains are assumed with isothermal grain growth. For medium carbon steel, the volume fraction X_{drx} of DRX is a function of the thermal–mechanical coupling action time t [29]:

$$X_{drx} = 1 - \exp[-0.693(\frac{t}{t_{0.5}})^{1.5}] \tag{2}$$

$$t_{0.5} = k_{md} Z^{n_{md}} \exp(\frac{Q_{md}}{RT}) \tag{3}$$

where $t_{0.5}$ is the time when X_{drx} is 50%. R is the gas constant, and T is the current temperature of material. Z is the Zener-Hollomon parameter (a parameter summarizing deformation temperature and strain rate). It can be written as
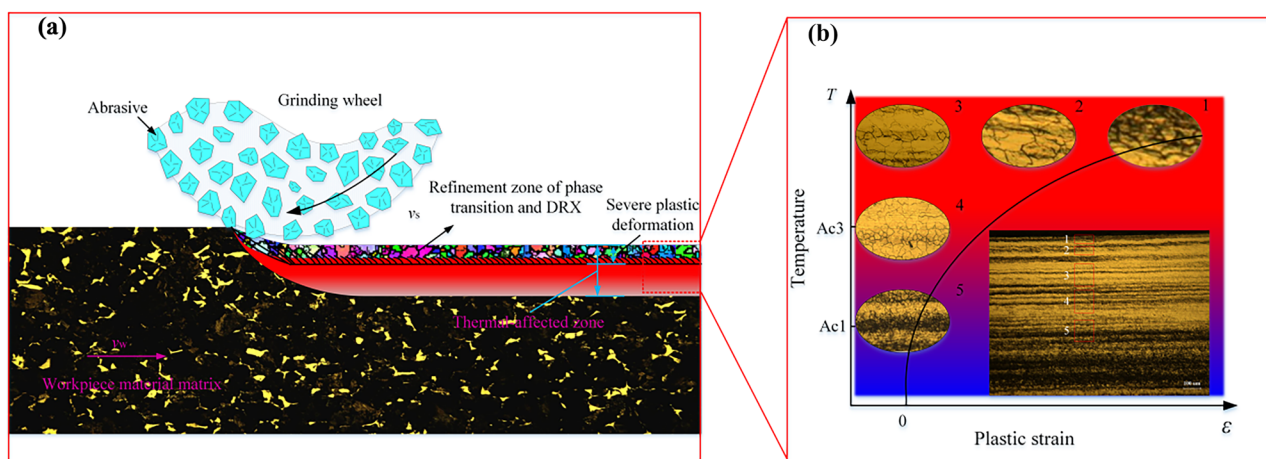
Fig. 1 **a** The grain refinement, SPD, and thermal influence mechanism of the grind-strengthening layer. **b** Temperature-deformation-microstructure map for 40Cr steel derived from grind-strengthening experiment and related analysis

$$Z = \dot{\varepsilon} \exp(\frac{Q_{\text{def}}}{RT}) \tag{4}$$

where $\dot{\varepsilon}$ is the strain rate and Q_{def} is the deformation activation energy. The size of DRX grain d_{drx} is obtained by Sellar's model as

$$d_{\text{drx}} = \varepsilon^{-0.5} d_0^{0.4} \exp(\frac{30000}{RT}) \tag{5}$$

where ε is the plastic strain and d_0 is the initial grain size. According to the simple mixture rule, the final grain size can be as follows:

$$d = d_{\text{drx}} X_{\text{drx}} + d_0 (1 - X_{\text{drx}}) \tag{6}$$

The material yield stress is constant for the traditional J–C model. In this study, the Hall–Petch equation can also relate yield strength to the average grain size as [30]

$$A = A_{\text{h-p}} + K_{\text{h-p}} d^{-0.5} \tag{7}$$

where A is the yield strength of material and $A_{\text{h-p}}$ and $K_{\text{h-p}}$ are coefficients of the Hall–Petch equation. Therefore, the modified J–C model considering the effect of grain size on yield stress can be used for the grind-strengthening process, which can be expressed as follows:

$$\sigma = (A_{\text{h-p}} + K_{\text{h-p}} d^{-0.5} + B\varepsilon^n)(1 + C \ln \frac{\dot{\varepsilon}}{\dot{\varepsilon}_0}) \left[1 - (\frac{T - T_0}{T_m - T_0})^m \right] \tag{8}$$

where B, C, m, and n are the material constants; T is the shear plane temperature; T_0 is the room temperature; and T_m is the melting temperature. The parameters of the 40Cr alloy steel–modified J–C model and material constants are described in Table 1.

3 Modified grinding force and temperature model

The methodology used in this study focuses on predicting grinding force and temperature considering microstructure evolution in the grinding process, which relies on the thermo-mechanical loadings applied onto the grinding contact area. Grinding force is a comprehensive macroscopic manifestation of the interaction between the abrasive grains and workpiece. It can lead to high grinding heat, plastic deformation, and microstructure evolution. Because grinding force is a large amount of negative rake angle abrasive grains to participate in removal. Therefore, the study of single abrasive cutting force can be the basic research of macro-grinding force [31]. Many studies have shown the cutting force of the single abrasive grain is superimposed with three-stage: chip formation, plowing, and rubbing forces. The geometry structure of abrasive grain is assumed as a cone with the cone tip flattened as exhibited in Fig. 2.

As shown in Fig. 2, when the undeformed chip thickness h is very small, the grinding force is mainly composed of rubbing and plowing force. The chip formation force is generated when the interference depth is greater than the critical chip thickness h_c. Single abrasive grain cutting can be simplified to two-dimensional orthogonal cutting. The rubbing force is produced by the elastic or elastic–plastic contact between the abrasive wear plane and workpiece [32]. It can be obtained by the integral of normal stress and shear stress in a fixed length:

$$\begin{cases} F_{\text{tg,rubbing}} = b \int_0^{L_{\text{VB}}} \tau_{\text{w}}(x) dx \\ F_{\text{ng,rubbing}} = b \int_0^{L_{\text{VB}}} \sigma_{\text{w}}(x) dx \end{cases} \tag{9}$$

where

$$b = \begin{cases} 2r \cos \alpha & h < h_n \\ 2(r \cos \alpha_n + (h - h_n)/\tan(-\alpha)) & h \geq h_n \end{cases} \tag{10}$$
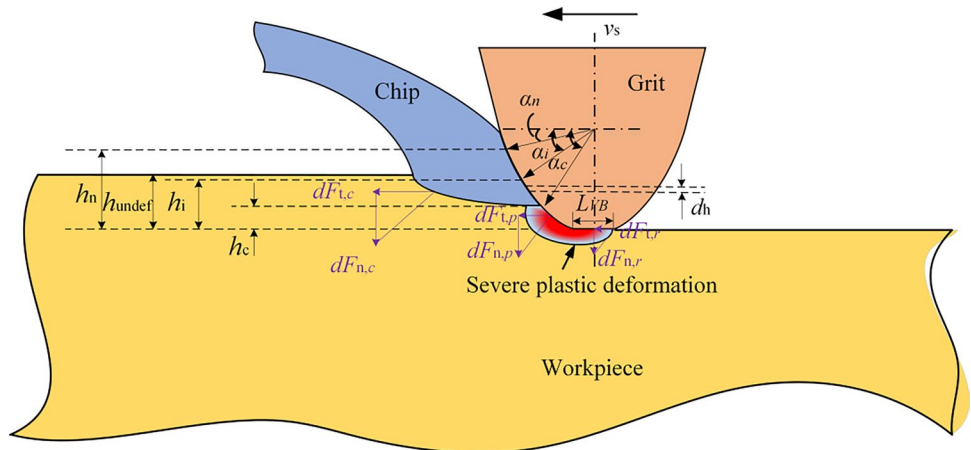
$$\begin{cases} \sigma_w(x) = \sigma_0((L_{VB} - x)/L_{VB})^2 \text{ for } 0 < x < L_{VB} \\ \tau_w(x) = \tau_0 \text{ for } 0 < x < L_{VB}(1 - \sqrt{\tau_0/\sigma_0}) \\ \tau_w(x) = \mu(\sigma_w(x)) \text{ for } L_{VB}(1 - \sqrt{\tau_0/\sigma_0}) < x < L_{VB} \end{cases} \tag{11}$$

where L_{VB} is the abrasive top friction length. μ is the friction coefficient. b is the contact width between the abrasive grain and specimen. h_n, α, and α_n are the nominate undeformed chip thickness, the geometric rake, and the nominated rake angle, respectively. τ_w and σ_w are the shear stress and the normal stress. The σ_0 and τ_0 can be decided by the procedure parameters:

Table 1 Material constants for 40Cr [25]

Parameters	A (MPa)	$A_{\text{h-p}}$ (MPa)	$K_{\text{h-p}}$ (MPa)	B (MPa)	C	m	n	T_0 (℃)
Values	785	574	112	540	0.0124	1.18	0.29	20
Parameters	T_m (℃)	k_{md}	n_{md}	Q_{md} (kJ/mol)	Q_{def} (kJ/mol)	R	d_0 (μm)	$\dot{\varepsilon}_0 (\text{s}^{-1})$
Values	1500	2.5	−0.8	230	171	8.314	25	1

Fig. 2 Interference model of single grit and workpiece

$$\begin{cases} \sigma_0 = k_0 \left(1 + \frac{\pi}{2} - 2\rho_0 - 2\varphi + 2\gamma + \sin(2\gamma - 2\varphi) \right) \\ \tau_0 = k_0 \cos(2\gamma - 2\varphi) \\ \gamma = \eta_{\mathrm{p}} + \varphi - \sin^{-1}\left(\sqrt{2}\sin(\rho_0)\sin(\eta_{\mathrm{p}}) \right) \\ \eta_{\mathrm{p}} = 0.5\cos^{-1}(\mu) \end{cases} \quad (12)$$

where ρ_0 is the prow angle of the workpiece directly in front of the abrasive grain, and it can be set to zero since the cutting width is much larger than the contact thickness [33]. When the abrasive grains start to cut, a small amount of material accumulate at the front of the abrasive grains, and a large amount of material accumulates on both sides of the abrasive grains. At this time, it is in the plowing state. The contact state is alike to the Brinell indentation experiment. As a result, the plowing force may be estimated using the indentation force function in the normal direction in the direction of the critical rake angle half. In addition, there is also friction. Hence, the normal and tangential plowing force can be expressed as

$$\begin{cases} F_{\mathrm{tg,plowing}} = F_{\mathrm{p}}\left(\sin\left(\frac{\alpha_c}{2} \right) + \mu\cos\left(\frac{\alpha_c}{2} \right) \right) \\ F_{\mathrm{ng,plowing}} = F_{\mathrm{p}}\left(\cos\left(\frac{\alpha_c}{2} \right) + \mu\sin\left(\frac{\alpha_c}{2} \right) \right) \end{cases} \quad (13)$$

where α_c is the critical rake angle. F_{p} can be calculated by the Brinell hardness-pressure equation:

$$F_{\mathrm{p}} = 2\pi rhHB \quad (14)$$

When h is greater than h_c, that is, when the actual rake angle is greater than a_c, the chip generation stage can be entered. Therefore, according to the change of h, the cutting force can be expressed in two stages:

$$\begin{cases} F_{\mathrm{tg,chip}} = \int_{\alpha_c}^{\alpha_s} \frac{\tau\cos(\beta-\alpha)}{\sin\varphi\cos(\varphi+\beta-\alpha)} 2r^2\cos^2\alpha d\alpha \\ F_{\mathrm{ng,chip}} = \int_{\alpha_c}^{\alpha_s} \frac{\tau\sin(\beta-\alpha)}{\sin\varphi\cos(\varphi+\beta-\alpha)} 2r^2\cos^2\alpha d\alpha \end{cases} \quad h_c < h < h_n \quad (15)$$

$$\begin{cases} F_{\mathrm{tg,chip}} = \int_{\alpha_c}^{\alpha_n} \frac{\tau\cos(\beta-\alpha)}{\sin\varphi\cos(\varphi+\beta-\alpha)} 2r^2\cos^2\alpha d\alpha + \\ \quad \int_{h_n}^{h} \frac{2\tau(r\cos\alpha_n + (h-h_n)/\tan(-\alpha))\cos(\beta-\alpha_n)}{\sin\varphi\cos(\varphi+\beta-\alpha_n)} dh \\ F_{\mathrm{ng,chip}} = \int_{\alpha_c}^{\alpha_n} \frac{\tau\sin(\beta-\alpha)}{\sin\varphi\cos(\varphi+\beta-\alpha)} 2r^2\cos^2\alpha d\alpha + \\ \quad \int_{h_n}^{h} \frac{2\tau(r\cos\alpha_n + (h-h_n)/\tan(-\alpha))\sin(\beta-\alpha_n)}{\sin\varphi\cos(\varphi+\beta-\alpha_n)} dh \end{cases} \quad h > h_n \quad (16)$$

where τ is the shear flow stress, which can be obtained by Eq. (18). β is the friction angle. φ is the shear angle. r is the grain radius. The β and φ can be acquired by

$$\begin{cases} \varphi = \frac{\pi}{4} - \frac{\beta}{2} + \frac{\alpha}{2} \\ \beta = \arctan\mu \end{cases} \quad (17)$$

The shear flow stress of workpiece material can be calculated by the modified J–C model of Eq. (8), which is as follows:
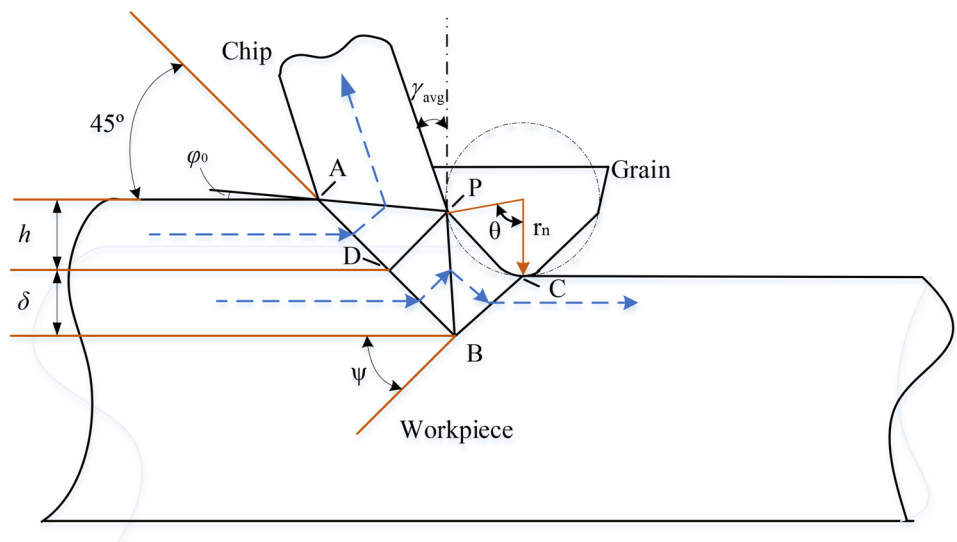
$$\tau = \frac{1}{\sqrt{3}}(A_{\mathrm{hp}} + K_{\mathrm{hp}}d^{-0.5} + B\varepsilon^n)(1 + C\ln\frac{\dot{\varepsilon}}{\dot{\varepsilon}})\left[1 - \left(\frac{T-T_0}{T_{\mathrm{m}}-T_0} \right)^m \right] \quad (18)$$

From the above analysis, the shear flow stress depends on the material constitutive parameters, plastic strain, strain rate, and temperature during machining. Therefore, the solution of plastic strain and strain rate is necessary. In this study, due to the material being removed by a negative rake angle tool during the grinding process, the strain and strain rate can be calculated by utilizing a model based on slip line analysis [26]. The schematic for the deformation analysis of material in grinding is illustrated in Fig. 3.

The total strain of the deformation material can be calculated according to the weighting of the deformation area of the chip and machined surface, as follows:

Fig. 3 Geometric model of material slip in cutting

$$\varepsilon = \frac{1}{\sqrt{3}} \left(\frac{\upsilon_{\text{chip}} \gamma_{\text{chip}} + \upsilon_{\text{workpiece}} \gamma_{\text{workpiece}}}{\upsilon_{\text{chip}} + \upsilon_{\text{workpiece}}} \right) \quad (19)$$

The shear strains of the chip and matrix are, respectively, expressed as

$$\gamma_{\text{chip}} = \frac{\sqrt{2} \sin \theta_{\text{PD}}}{\sin \left(\pi/4 + \theta_{\text{PD}} \right)} + \frac{\cos \left(\gamma_{\text{avg}} + \theta_{\text{PD}} \right)}{\cos \left(\gamma_{\text{avg}} - \varphi_0 \right) \sin \left(\varphi_0 + \theta_{\text{PD}} \right)} \quad (20)$$

$$\gamma_{\text{workpiece}} = \frac{\sqrt{2} \sin \theta_{\text{PD}}}{\sin \left(\pi/4 + \theta_{\text{PD}} \right)} + \frac{\sin \left(\theta_{\text{PD}} + \theta/2 \right)}{\sin \left(\theta_{\text{PB}} + \theta/2 \right) \sin \left(\theta_{\text{PD}} + \theta_{\text{PB}} \right)} + \frac{\sin(\theta/2)}{\sin(\psi) \sin \left(\psi + \theta/2 \right)} \quad (21)$$

where υ_{chip} and $\upsilon_{\text{workpiece}}$ are deformation area weights for chip and matrix, and γ_{avg} is the average rake angle. $\theta_{\text{PD}}, \theta_{\text{PB}}$, and ψ are the inclination angles of PD, PB, and BC, respectively. These parameters can be obtained by geometrical relationships.

In the same way, a weighting function is applied to derive the total strain rate from the strain rates of the chip and matrix:

$$\dot{\varepsilon} = \frac{1}{\sqrt{3}} \left(\frac{\upsilon_{\text{chip}} \dot{\gamma}_{\text{chip}} + \upsilon_{\text{workpiece}} \dot{\gamma}_{\text{workpiece}}}{\upsilon_{\text{chip}} + \upsilon_{\text{workpiece}}} \right) \quad (22)$$

$$\dot{\gamma}_{\text{chip}} = 2v_s \frac{\gamma_{\text{chip}}}{\sqrt{2} \sin \left(\pi/4 + \theta_{\text{PD}} \right) \overline{PD}} \quad (23)$$

$$\dot{\gamma}_{\text{workpiece}} = 2v_s \frac{\gamma_{\text{workpiece}}}{\sqrt{2} \sin \left(\pi/4 + \theta_{\text{PD}} \right) \overline{PD} + \frac{\sin (\psi + \theta/2)}{\sin \psi} \overline{PC}} \quad (24)$$

where v_s is the abrasive linear velocity, $\overline{PD}$ and $\overline{PC}$ are the lengths of PD and PC, respectively. The strains and strain rates can be applied to calculate the shear flow stress by Eq. (18). Then, the cutting force of a single grit can be calculated. The total cutting force of a single abrasive grain is the sum of rubbing, plowing, and chip formation force, respectively. It can be expressed by

$$\begin{cases} F_{\text{tg,total}} = F_{\text{tg,chip}} + F_{\text{tg,plowing}} + F_{\text{tg,rubbing}} \\ F_{\text{ng,total}} = F_{\text{ng,chip}} + F_{\text{ng,plowing}} + F_{\text{ng,rubbing}} \end{cases} \quad (25)$$

The total grinding force of a single abrasive grain is directly related to the undeformed chip thickness. In addition, the regions where the abrasive grains come into touch with the workpiece are non-uniform during the grind strengthening. In this study, it can be assumed that the undeformed chip thickness of abrasive grains obeys the Rayleigh probability density function as followed by [34]

$$f(h) = \begin{cases} \frac{h}{\varsigma} \exp \left(-\frac{h^2}{2\varsigma^2} \right) & h \geq 0 \\ 0 & h \leq 0 \end{cases} \quad (26)$$

where ς is the function of the machining parameters, which can be written as

$$\varsigma = \sqrt{\frac{a_p v_w}{2 v_s l_c C_d \tan \left(\overline{\theta} \right)} - \frac{h_c^2}{2}} \quad (27)$$

where a_p is grinding depth, v_w is the feed speed of workpiece, v_s is the wheel velocity, and $l_c = \sqrt{a_p d_s}$ is the real contact length of grinding zone. $2\bar{\theta}$ is the cone angle of abrasive grains and C_d is the dynamic grain density. Therefore, the average grinding force can be expressed by

$$\begin{cases} E(F_{tg,total}) = \int_0^\infty f(h) F_{tg,total}(h) dh \\ E(F_{ng,total}) = \int_0^\infty f(h) F_{ng,total}(h) dh \end{cases} \tag{28}$$

Then the average grinding force of single grain is multiplied by the number of active cutting blades to obtain the total grinding force:

$$\begin{cases} F_t = C_d b_s l_c E(F_{tg,total}) \\ F_n = C_d b_s l_c E(F_{ng,total}) \end{cases} \tag{29}$$

where F_t and F_n are the macro-tangential and normal grinding forces, respectively. b_s is the actual grinding width.

To summarize, the grinding force model considering the microstructure evolution has been established. According to this model, the grinding force can be predicted.

The grinding temperature is the essential reason for the microstructure modification of the ground superficial layer during the grind-strengthening process. In this section, the predicted grinding force obtained by the above analysis can be applied to predict the average heat flux density in the grinding contact zone by

$$q_0 = \frac{\eta F_t v_s}{l_c b_s} \tag{30}$$

$$\eta = \frac{1}{1 + \sqrt{(k\rho c)_s / (k\rho c)_w}} \tag{31}$$

where $(k\rho c)_s$ and $(k\rho c)_w$ are the thermos-physical parameters of wheel and workpiece, respectively. The triangular moving heat source is widely incorporated in the temperature field calculation of surface grinding. The heat flux density can be written as

$$q(x') = q_0(1 + \frac{2}{l_g} x') \tag{32}$$

The moving heat source model of a two-dimensional solution can be proposed to the problem of plane grinding temperature field, which is extremely valuable in heat transfer problems in mechanical engineering. The general equation for heat conduction is as follows [36]:

$$k\left(\frac{\partial^2 T}{\partial x^2} + \frac{\partial^2 T}{\partial z^2}\right) = \rho c\left(\frac{\partial T}{\partial t} - v_w \frac{\partial T}{\partial x}\right) \tag{33}$$

where $T = T(x, z, t)$ notes the temperature is spatially and temporally dependent on x, z, and t, respectively. c is the specific heat capacity, k is the thermal conductivity, ρ is the material density, and v_w is the feed rate. The initial temperature is set to 20 ℃. Table 2 lists the thermal–mechanical parameters of 40Cr.

Assuming that the heat transfer surface is adiabatic in the semi-infinite region, the solution of the differential equation (Eq. (33)) can be expressed by [37]

$$T(x, z, x', t, t') = \frac{aQ_w}{k} \left\{ \frac{2}{[4\pi a(t - t')]^{3/2}} e^{-\frac{[(x-x')+v_w(t-t')]^2 + z^2}{4a(t-t')}} \right. $$
$$\left. - \frac{h_{trans}}{4\pi a k(t - t')} \mathrm{erfc}\left(\frac{z}{2\sqrt{a(t-t')}} + \frac{h_{trans}}{k}\sqrt{a(t-t')}\right) \cdot e^{\frac{z h_{trans}}{k} + a(t-t') \times (\frac{h_{trans}}{k})^2} e^{-\frac{[(x-x')+v_w(t-t')]^2}{4a(t-t')}} \right\} \tag{34}$$

where F_t is the tangential grinding force. For the plane dry grinding, R is the heat distribution ratio, which can be expressed by [35]

where $a = k/\rho c$ is the heat diffusivity, $Q_w = q(x')dx'dt'$ is the heat input, and h_{trans} is the heat transfer coefficient. Through integral and dimensionless processing of Eq. (34), the temperature can be written as

$$T(X, Z, t) = \frac{2aq_0}{\sqrt{\pi} k v_w} \int_0^{\frac{v_w \sqrt{t}}{2\sqrt{a}}} e^{-\frac{Z^2}{4\zeta^2}} \cdot \left\{ \left[1 + \frac{X + 2\zeta^2}{L}\right] \left[\mathrm{erf}\left(\frac{X+L}{2\zeta} + \zeta\right) - \mathrm{erf}\left(\frac{X-L}{2\zeta} + \zeta\right)\right] \right.$$
$$\left. + \frac{2\zeta}{L\sqrt{\pi}} \left[e^{-\left(\frac{X+L}{2\zeta} + \zeta\right)^2} - e^{-\left(\frac{X-L}{2\zeta} + \zeta\right)^2}\right] \right\} d\zeta - \frac{2aq_0}{k v_w} H \int_0^{\frac{v_w \sqrt{t}}{2\sqrt{a}}} \zeta e^{HZ + H^2 \zeta^2} \mathrm{erfc}\left(\frac{Z}{2\zeta} + H\zeta\right)$$
$$\times \left\{ \left[1 + \frac{X + 2\zeta^2}{L}\right] \left[\mathrm{erf}\left(\frac{X+L}{2\zeta} + \zeta\right) - \mathrm{erf}\left(\frac{X-L}{2\zeta} + \zeta\right)\right] + \frac{2\zeta}{L\sqrt{\pi}} \left[e^{-\left(\frac{X+L}{2\zeta} + \zeta\right)^2} - e^{-\left(\frac{X-L}{2\zeta} + \zeta\right)^2}\right] \right\} d\zeta \tag{35}$$

Table 2 Thermal–mechanical property constants of 40Cr

Density ρ (kg/m^3)	Thermal expansion coefficient ($^\circ$C^{-1})	Young's modulus E (GPa)	Specific heat capacity c (J/kg·$^\circ$C)	Thermal conductivity k (W/m·$^\circ$C)
7850	24.82	206	467	41.84

In Eq. (35), the dimensionless treatment of variables is as follows:

$$\zeta = \frac{v_w \sqrt{t-t'}}{2\sqrt{a}}, X = \frac{v_w x}{2a}, Z = \frac{v_w z}{2a}, L = \frac{v_w}{4a}, H = \frac{2ah_{trans}}{kv_w}$$
(36)

Through the above-mentioned temperature field model, the grinding temperature field can be solved analytically.

4 Experiments and model validations

4.1 Experiment set-up of grind strengthening

40Cr steel and white corundum wheel (WA46L5v) are used in grind-strengthening experiments as workpiece and the grinding tool, respectively. The workpiece material is composed of pearlite and ferrite as shown in Fig. 4. The chemical element composition of the workpiece material is shown in Table 3. Grind-strengthening experiments are carried out on M7120A. The grind-strengthening experiment site and equipment are shown in Fig. 5. During grind-strengthening processes, the grinding forces were achieved by the Kistler 3-axis dynamometer (Kistler 9257B). The

top-type thermocouple is applied to measure the grinding temperature of the 3 mm below the ground surface to verify the accuracy of analytical temperature field calculation. Firstly, the grinding strengthening layer is exposed by wire cutting. Then, the tested superficial layer is polished to the corrosion requirements. The saturated picric acid solution and 4% nitric acid alcohol solution are applied to obtain the prior austenite grains and martensite microstructure, respectively. The characterizations of the grind-strengthening layer microstructure are observed with a Leica DMI5000M optical metallographic microscope. The applied grinding parameters are listed in Table 4.

4.2 Microstructure modification of grinding strengthening layer

Figure 6 illustrates the observation of the grind-strengthening layer microstructure inspected from the longitudinal sections. Figures 6a, b are the martensite microstructures obtained by corrosion of an alcohol solution containing 4 vol% nitric acids to observe the phase transformation distribution. Figure 6c, d are corroded by supersaturated picric acid solution, and the purpose is to gain the prior austenite grains. It can judge the gradient microstructure refinement mechanism of the grind-strengthening layer through the prior austenite grains. It can be seen that austenite and martensite transformation occur during the grind-heating stage and cooling stage after grinding, respectively, in the ground superficial layer. The grain unit of the martensite structure is a lath sub-crystalline structure, and the size of the lath unit has a crucial influence on the strength and stiffness of the material. The size of the martensitic lath and prior austenite grains is proportional [38]. The driving
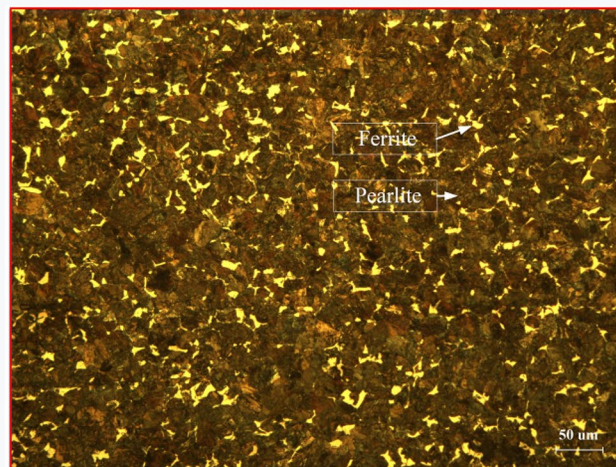
Fig. 4 Optical microscope observation of the initial organization of 40Cr steel

Table 3 Chemical composition of the 40Cr steel (wt.%)

Element	C	Si	Mn	Cr	Ni	P	S	Cu	Mo	Fe
Component%	0.37–0.44	0.17–0.37	0.50–0.80	0.80–1.10	≤0.30	≤0.035	≤0.035	0.030	0.10	Balance

force of martensite transformation can be elevated by the DRX of austenite grains. [27] Therefore, the wear resistance and fatigue resistance of the material can be significantly improved [28]. From Fig. 6b–d, due to the SPD, elevated temperature, and high cooling rate near the ground surface, the austenite dynamic recrystallization transformation in the grinding heating stage happens to form an equiaxed prior austenite grain refinement layer. Finally, the quenching process is realized by air cooling, so as to achieve a martensitic strengthening layer with a gradient grain refinement structure. The refine-grained martensitic structure can exhibit excellent strength, as well as high toughness.

4.3 Grinding force and temperature verification

The thermal–mechanical-influenced material undergoes microstructure phase transformation and dynamic recrystallization during grind strengthening. The grain refinement of material microstructure can have an important effect on the material flow stress and grinding force. The grind-strengthening experiments have been implemented to verify the applicability of the current modified J-C and traditional J-C models. Figure 7 depicts the execution of the prediction program. The grinding forces of predicted and experimental are displayed in Fig. 8.

Figure 8 summarizes the grinding forces of experimental, the predicted by traditional, and modified J–C model under different grinding parameters. The modified J–C model

based on the dynamic recrystallization can achieve a smaller prediction error for the grinding force compared with the traditional J–C model from Fig. 8. This is due to the grain refinement of the material microstructure caused by the thermo-mechanical coupling during the grind-strengthening process, which changes the material plastic deformation characteristics. The material flow stress has a strong correlation with the change of grain size as a result of DRX transformation [39], and it has a more profound consideration of the removal mechanism of the material 40Cr under high heat and severe plastic deformation. Therefore, the prediction accuracy of the macroscopic grinding force is improved.

Figure 9 compares the experimental results with the predicted grinding forces by traditional J-C and modified J-C models. It can be seen that the predictions of the grinding force by the two models are consistent and positively correlated with the variation of process parameters. The predicted grinding forces considering the microstructure evolution match better with the experimental results. According to the experimental and prediction results, it can be statistically obtained that the prediction errors of the traditional J–C model for the tangential and normal forces are 21% and 15.2%, which are both greater than 11.3% and 6.67% of the improved J–C model. It is evident that the improved J–C model accurately predicts the grinding forces based on the microstructure evolution.

The top-type thermocouple is applied to measure the temperature about 3 mm below grinding surface. The
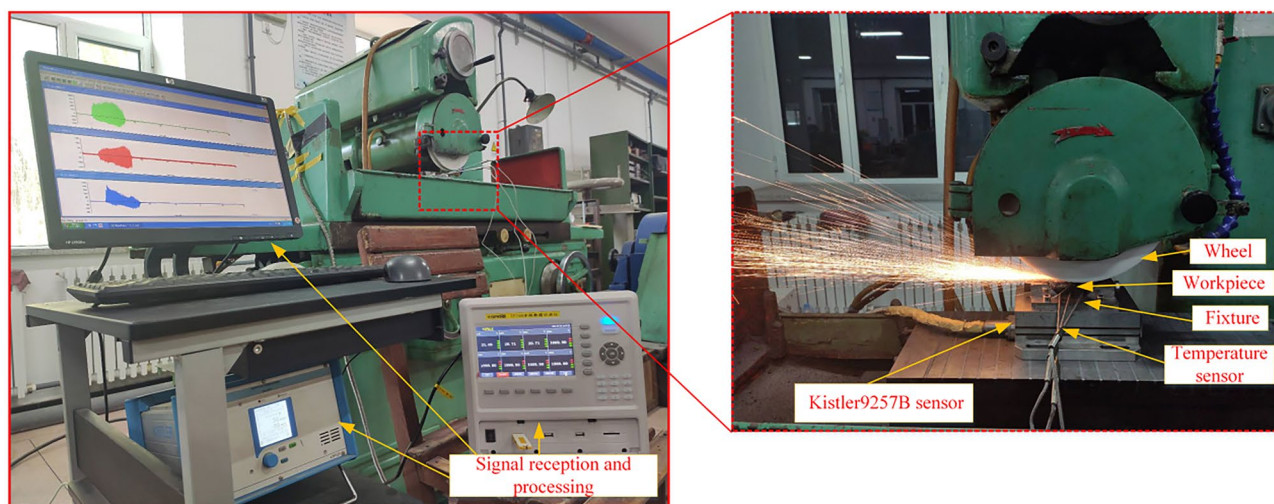
Fig. 5 Experimental setup of grind strengthening

Table 4 The parameters of grind-strengthening process

| Grinding case no.	Grinding depth a_p (μm)	Workpiece feed speed v_w (m/s)	Wheel speed v_s (m/s)
1	150	0.02	30
2	200	0.02	
3	250	0.02	
4	200	0.01	
5	200	0.03	

grinding temperature analytical solution considering the microstructure evolution can be verified. The results of the analytical model and experimental match well as shown in Fig. 10a under the grinding parameter of ($a_p = 200$ μm, $v_w = 0.03$ m/s, and $v_s = 30$ m/s). It can be noted that the predicted results by triangular moving heat source are consistent with the experiment results. Furthermore, the

temperature field of the ground superficial layer is predicted by the solution of the temperature field. As illustrated in Fig. 10, the temperature of the ground surface reaches 974 ℃, which far exceeds the austenite transformation temperature. A grinding temperature of 782 ℃ is achieved (higher than the starting temperature of austenitizing Ac1 = 780 ℃) when the depth is at 400 μm. At a depth of 250 μm, the grinding temperature rises to 843 ℃. That is close to the final austenitizing temperature (Ac3 = 840 ℃). A 400μm martensite transformation layer is obtained through air cooling. The predicted phase transformation layer is in accordance with the thickness of the metallographic structure of Fig. 10b. As a result, the temperature investigation based on the grinding force considering material microstructure evolution supplies theoretical support for the study of quenching penetration depth in the grind-strengthening process.

a_p=200um, v_s=30m/s, v_w=0.03m/s
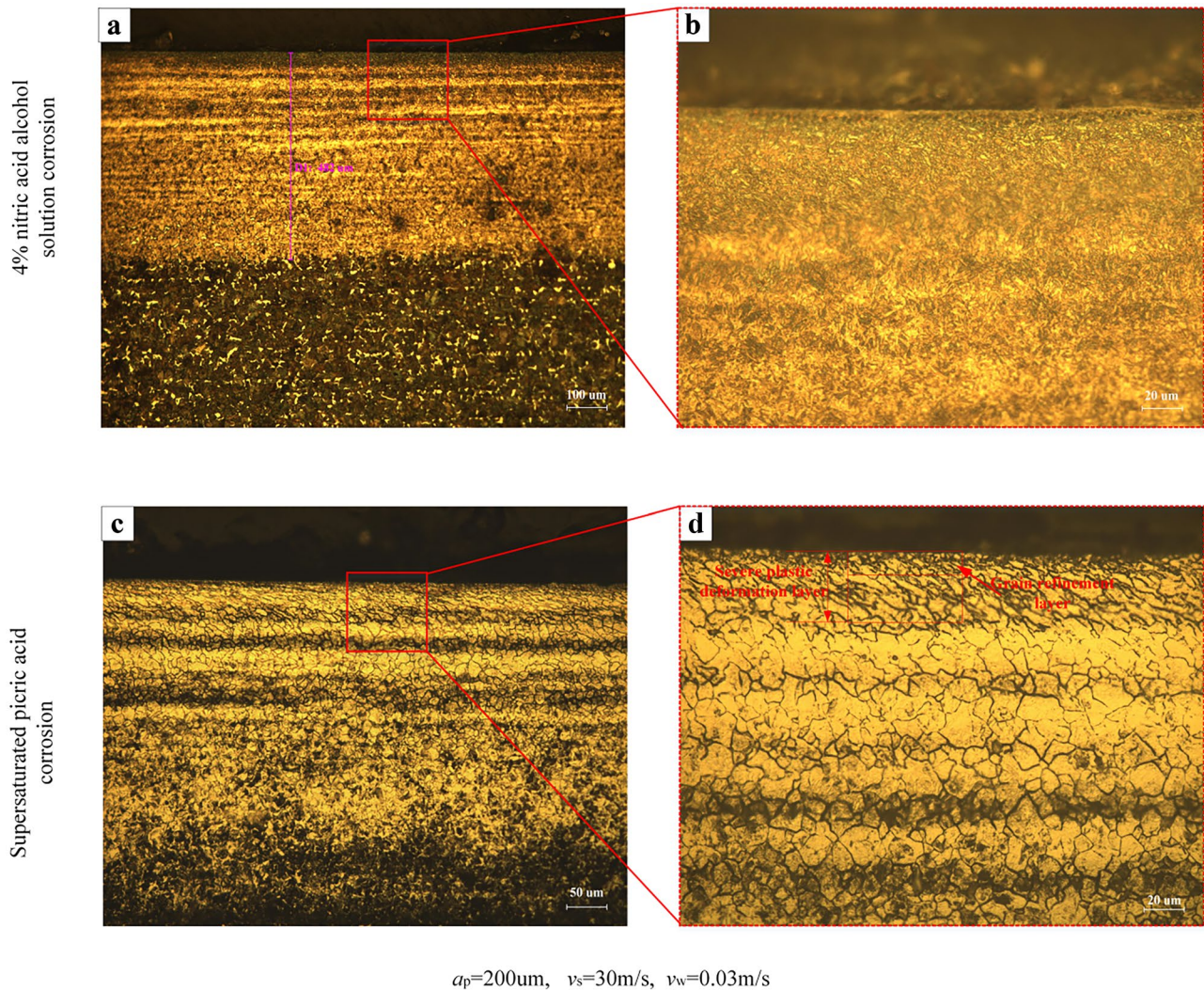
Fig. 6 Optical microscope metallographic observation of the grind-strengthening layer cross-section

Fig. 7 Grinding force and heat prediction program
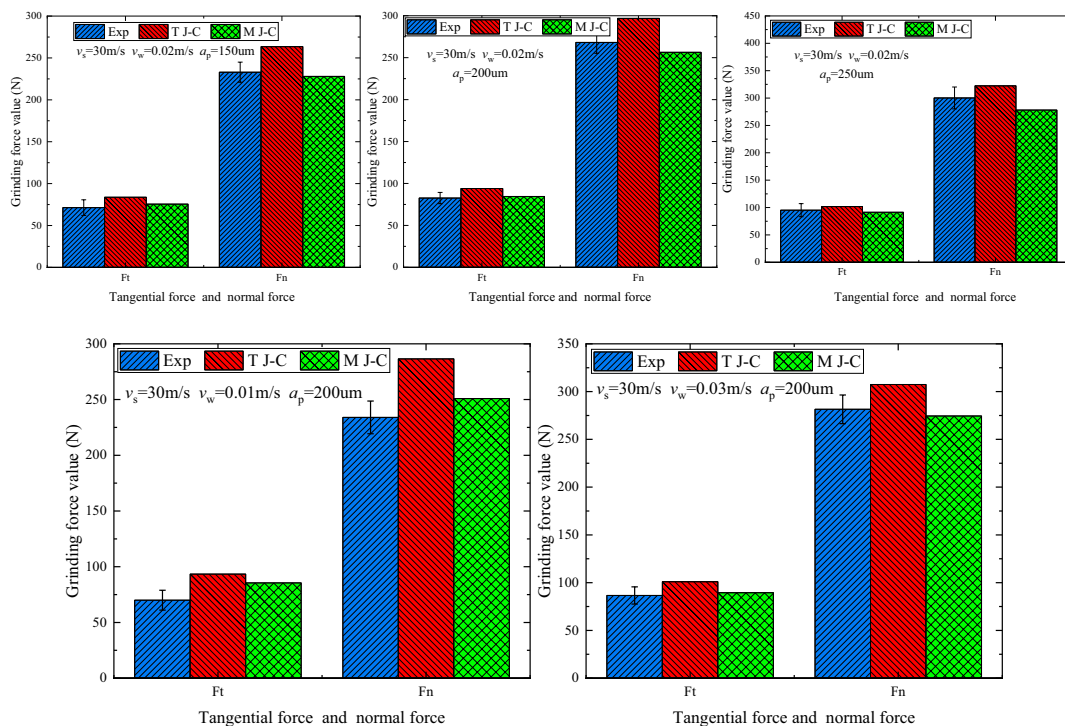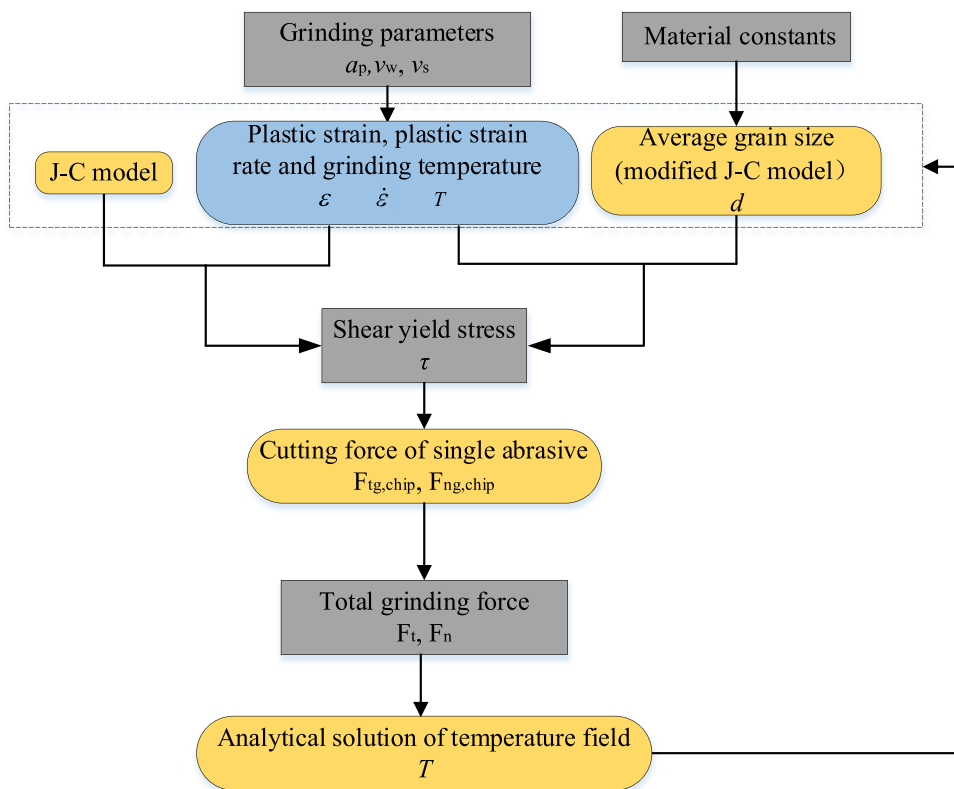
Fig. 8 The tangential and normal grinding force at different process parameters
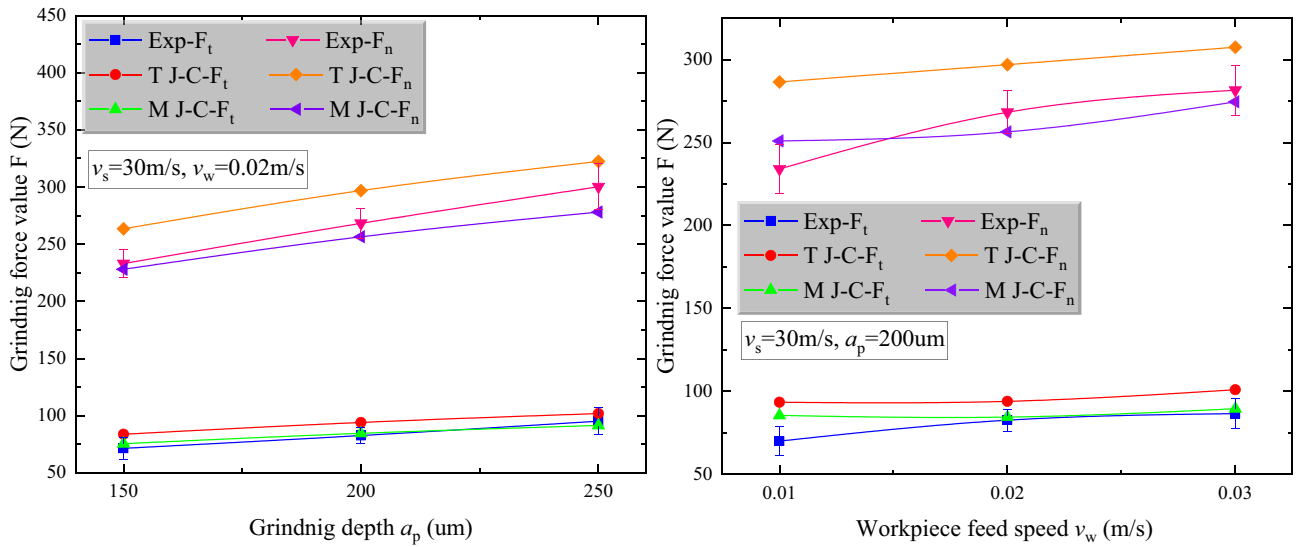
Fig. 9 Experimental and predicted grinding force changes under grinding parameters
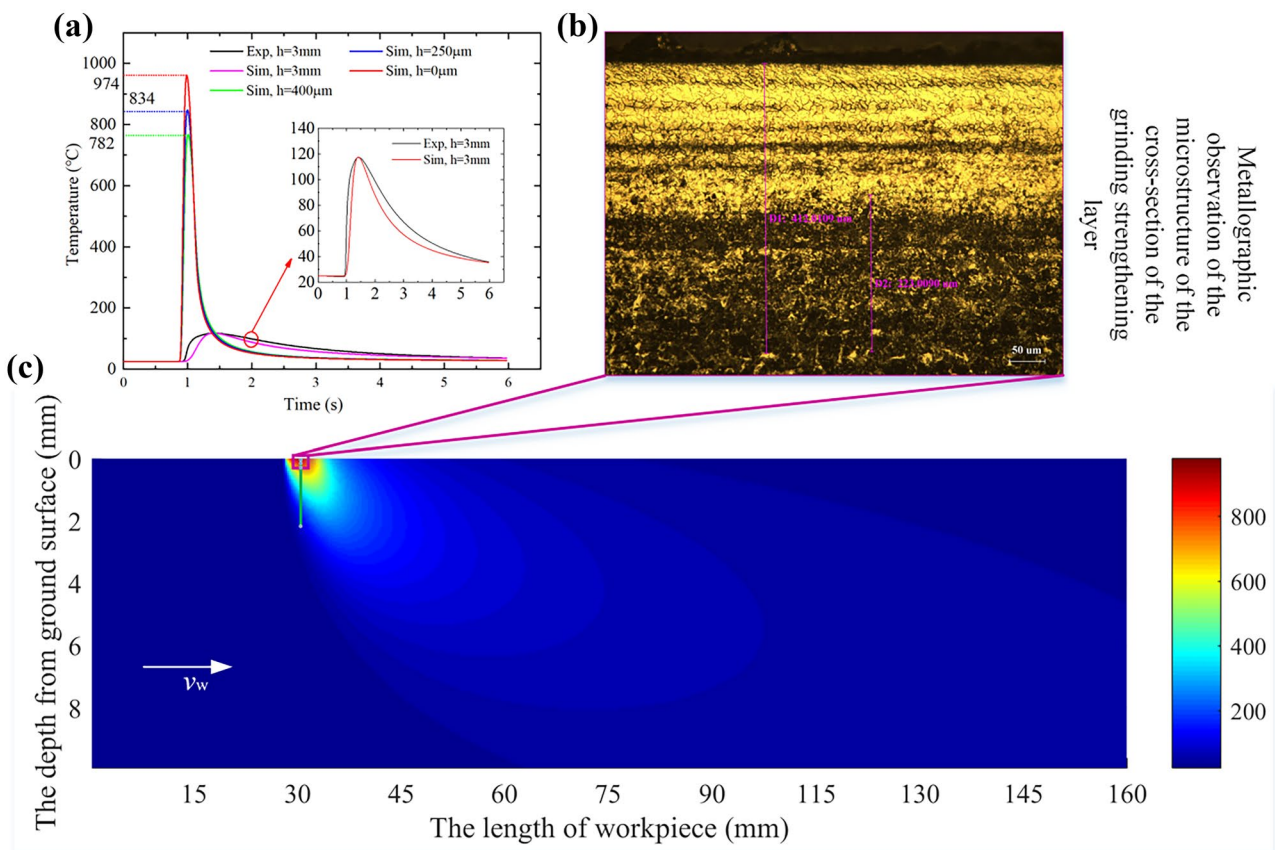

Fig. 10 Simulation and experimental temperature field of grind-strengthening layer section

5 Conclusions

The metallurgical behavior of material microstructure has a strong correlation with its flow stress during the hot deformation of grind-strengthening process. In view of solving the problem of the influence of phase transformation and DRX behavior introduced by high temperature and severe plastic deformation on grinding force and temperature of 40Cr steel during the grind-strengthening process, a modified J-C constitutive equation of 40Cr was established to predict the macroscopic grinding force and temperature combined with the JMAK model. Then grind-strengthening experimental verification was carried out. The specific conclusions can be obtained as follows:

1. Through the analysis of the chip formation force of grinding by the two established material constitutive models, the grinding force can be predicted effectively. The prediction errors of tangential and normal grinding forces with the traditional J–C model are 21% and 15.2%, respectively. The modified J–C model considering the microstructure evolution has prediction errors of 11.3% and 6.67%. Therefore, the modified J–C model based on the microstructure evolution has higher accuracy in predicting the grinding force. This provides a theoretical basis for optimizing the grind-strengthening process.

2. The temperature field of grinding strengthening layer obtained by the analytical model considering microstructure DRX behavior is in accordance with the results of the experiments. According to the obtained temperature field and the observation of the grinding strengthening microstructure, the grinding strengthening mechanism is caused by the austenitization and DRX of the material. The driving force of martensite transformation can be increased by refinement of prior austenite, therefore improving the hardenability of the part surface. Refined austenite is a sufficient condition for the formation of fine lath martensite. Finally, a microstructure-modified layer is formed, which presents a grain-refined martensitic structure. It can greatly improve the surface strength and wear resistance of parts.

References

1. Sun C, Hong Y, Xiu S, Yao Y (2021) Grain refinement mechanism of metamorphic layers by abrasive grinding hardening. J Manuf Process 69:125–141. https://doi.org/10.1016/j.jmapro.2021.07.040

2. Wang Y, Deng Y, Xiu S (2018) Study on the dynamic recrystallization mechanism during pre-stress dry grinding. J Manuf Process 32:100–109. https://doi.org/10.1016/j.jmapro.2018.01.021

3. Imbrogno S, Rinaldi S, Umbrello D et al (2018) A physically based constitutive model for predicting the surface integrity in machining of Waspaloy. Mater Des 152:140–155. https://doi.org/10.1016/j.matdes.2018.04.069

4. Sun C, Xiu SC, Li QL et al (2021) Mechanism of surface creation for dynamic and static feature end grinding of associated systems. Surf Technol 50:35–43

5. Dang J, Zhang H, An Q et al (2021) Surface integrity and wear behavior of 300M steel subjected to ultrasonic surface rolling process. Surf Coat Technol. https://doi.org/10.1016/j.surfcoat.2021.127380

6. Brockhoff T, Brinksmeier E (1999) Grind-hardening: a comprehensive view. CIRP Ann Manuf Technol 48:255–260. https://doi.org/10.1016/S0007-8506(07)63178-3

7. Zarudi I, Zhang LC (2002) Modelling the structure changes in quenchable steel subjected to grinding. J Mater Sci 37:4333–4341. https://doi.org/10.1023/A:1020652519141

8. Zarudi I, Zhang LC (2002) Mechanical property improvement of quenchable steel by grinding. J Mater Sci 37:3935–3943. https://doi.org/10.1023/A:1019671926384

9. Chen L, Sun W, Lin J et al (2019) Modelling of constitutive relationship, dynamic recrystallization and grain size of 40Cr steel during hot deformation process. Res Phys 12:784–792. https://doi.org/10.1016/j.rinp.2018.12.046

10. Duan C, Zhang F, Qin S et al (2018) Modeling of dynamic recrystallization in white layer in dry hard cutting by finite element—cellular automaton method. J Mech Sci Technol 32:4299–4312. https://doi.org/10.1007/s12206-018-0828-y

11. Ding H, Shin YC (2012) A metallo-thermomechanically coupled analysis of orthogonal cutting of AISI 1045 steel. J Manuf Sci E T ASME. https://doi.org/10.1115/1.4007464

12. Shen N, Ding H (2014) Physics-based microstructure simulation for drilled hole surface in hardened steel. J Manuf Sci E T ASME 136:1–5. https://doi.org/10.1115/1.4027732

13. Ahmad E, Karim F, Saeed K et al (2014) Effect of cold rolling and annealing on the grain refinement of low alloy steel. IOP Conf Ser Mater Sci Eng. https://doi.org/10.1088/1757-899X/60/1/012029

14. Junior AMJ, Guedes LH, Balancin O (2012) Ultra grain refinement during the simulated thermomechanical-processing of low

carbon steel. J Market Res 1:141–147. https://doi.org/10.1016/s2238-7854(12)70025-x

15. Dang J, Zhang H, An Q et al (2021) Surface modification of ultrahigh strength 300M steel under supercritical carbon dioxide (scCO2)-assisted grinding process. J Manuf Process 61:1–14. https://doi.org/10.1016/j.jmapro.2020.11.001

16. Raof NA, Ghani JA, Haron CHC (2019) Machining-induced grain refinement of AISI 4340 alloy steel under dry and cryogenic conditions. J Market Res 8:4347–4353. https://doi.org/10.1016/j.jmrt.2019.07.045

17. Ding H, Shin YC (2012) Dislocation density-based modeling of subsurface grain refinement with laser-induced shock compression. Comput Mater Sci 53:79–88. https://doi.org/10.1016/j.commatsci.2011.08.038

18. Xu Y, Gong Y, Zhang W, et al (2022) Effect of grinding conditions on the friction and wear performance of Ni-based singlecrystal superalloy. Arch Civ Mech Eng 22:102. https://doi.org/10.1007/s43452-022-00423-7

19. Tsuji N, Maki T (2009) Enhanced structural refinement by combining phase transformation and plastic deformation in steels. Scripta Mater 60:1044–1049. https://doi.org/10.1016/j.scriptamat.2009.02.028

20. Zhang F, Duan C, Sun W, Ju K (2019) Effects of cutting conditions on the microstructure and residual stress of white and dark layers in cutting hardened steel. J Mater Process Technol 266:599–611. https://doi.org/10.1016/j.jmatprotec.2018.11.038

21. Pan Z, Shih DS, Tabei A et al (2017) Modeling of Ti-6Al-4V machining force considering material microstructure evolution. Int J Adv Manuf Technol 91:2673–2680. https://doi.org/10.1007/s00170-016-9964-7

22. Pan Z, Tabei A, Shih DS et al (2018) The effects of dynamic evolution of microstructure on machining forces. Proc Inst Mech Eng Part B J Eng Manuf 232:2677–2681. https://doi.org/10.1177/0954405417703430

23. Zhang XP, Shivpuri R, Srivastava AK (2014) Role of phase transformation in chip segmentation during high speed machining of dual phase titanium alloys. J Mater Process Technol 214:3048–3066. https://doi.org/10.1016/j.jmatprotec.2014.07.007

24. Ding Z, Sun G, Jiang X et al (2019) Predictive modeling of microgrinding force incorporating phase transformation effects. J Manuf Sci E T ASME. https://doi.org/10.1115/1.4043839

25. Yao Y, Xiu S, Sun C et al (2021) Investigation on grinding-induced dynamic recrystallization behavior of 40Cr alloy steel. J Alloy Compd 867:158773. https://doi.org/10.1016/j.jallcom.2021.158773

26. Manjunathaiah J, Endres WJ (2000) A new model and analysis of orthogonal machining with an edge-radiused tool. J Manuf Sci E T ASME 122:384–390. https://doi.org/10.1115/1.1285886

27. Wu BB, Wang XL, Wang ZQ et al (2019) New insights from crystallography into the effect of refining prior austenite grain size on transformation phenomenon and consequent mechanical properties of ultra-high strength low alloy steel. Mater Sci Eng A 745:126–136. https://doi.org/10.1016/j.msea.2018.12.057

28. Hidalgo J, Santofimia MJ (2016) Effect of prior austenite grain size refinement by thermal cycling on the microstructural features of as-quenched lath martensite. Metall Mater Trans A 47:5288–5301. https://doi.org/10.1007/s11661-016-3525-4

29. Hodgson P, Gibbs R (1992) A mathematical model to predict the mechanical properties of hot rolled C-Mn and microalloyed steels. ISIJ Int 32:1329–1338

30. Johnston TL, Feltner CE (1970) Grain size effects in the strain hardening of polycrystals. Metall Mater Trans 1:1161–1167. https://doi.org/10.1007/BF02900226

31. Gao T, Li C, Yang M et al (2021) Mechanics analysis and predictive force models for the single-diamond grain grinding of carbon fiber reinforced polymers using CNT nano-lubricant. J Mater Process Technol. https://doi.org/10.1016/j.jmatprotec.2020.116976

32. Shao Y, Li B, Chiang KN, Liang SY (2015) Physics-based analysis of minimum quantity lubrication grinding. Int J Adv Manuf Technol 79:1659–1670. https://doi.org/10.1007/s00170-015-6941-5

33. Smithey DW, Kapoor SG, DeVor RE (2001) A new mechanistic model for predicting worn tool cutting forces. Mach Sci Technol 5:23–42. https://doi.org/10.1081/MST-100103176

34. Younis MA, Alawi H (1984) Probabilistic analysis of the surface grinding process. Trans Can Soc Mech Eng 8:208–213. https://doi.org/10.1139/tcsme-1984-0031

35. Ramanath S, Shaw MC (1988) Abrasive grain temperature at the beginning of a cut in fine grinding. J Manuf Sci E T ASME 110:15–18. https://doi.org/10.1115/1.3187835

36. Foeckerer T, Zaeh MF, Zhang OB (2013) A three-dimensional analytical model to predict the thermo-metallurgical effects within the surface layer during grinding and grind-hardening. Int J Heat Mass Transf 56:223–237. https://doi.org/10.1016/j.ijheatmasstransfer.2012.09.029

37. Des Ruisseaux NR, Zerkle RD (1970) Thermal analysis of the grinding process. J Eng Ind 92:428–433. https://doi.org/10.1115/1.3427768

38. Galindo-Nava EI, Rainforth WM, Rivera-Díaz-del-Castillo PEJ (2016) Predicting microstructure and strength of maraging steels: elemental optimisation. Acta Mater 117:270–285. https://doi.org/10.1016/j.actamat.2016.07.020

39. Gholizadeh R, Shibata A, Tsuji N (2020) Grain refinement mechanisms in BCC ferritic steel and FCC austenitic steel highly deformed under different temperatures and strain rates. Mater Sci Eng A 790:139708. https://doi.org/10.1016/j.msea.2020.139708